Urban Temperature Simulation for resilient City Planning based on a single High Resolution Satellite Stereo Data Scene

Thomas Krauß[1], Pablo d’Angelo[1], Erwin Lindermeir[1], Chiara Richiardi[2], Markus Tum[3]

[1] German Aerospace Center (DLR), Earth Oberservation Center (EOC),
Münchener Str. 20, 82234 Oberpfaffenhofen, Germany, thomas.krauss@dlr.de
[2] Italian National Agency for New Technologies, Energy and Sustainable Economic Development (ENEA), Italy
[3] RIWA GmbH, An der Neumühle 5, 87700 Memmingen, Germany

Keywords: Temperature simulation, Urban heat island, Very high resolution satellite imagery, Dense digital elevation models, Classification of materials, Urban Digital Twin.

Abstract

Temperatures in urban areas are rising due to the climate change. Together with increasing urbanization and densification reducing cooling green spaces in cities this leads to so called urban heat islands (UHI) with increased surface- and air-temperatures in urban areas relatively to the surrounding areas. Since high temperatures are the reason for many exceed deaths municipalities are forced to protect their citizens. Satellite earth observation allows to monitor the development of urban heat islands to warn inhabitants early from dangerous heat. An other important way is increasing the resilience of cities to heat waves. For this we developed a simple but efficient method for the simulation of urban surface- and air-temperatures from single very high resolution stereo satellite images. In this paper we present the improved workflow for the simulation of urban temperatures together with the calibration and validation. Further we compare the results to in-situ-measurements in the city of Memmingen in southern Germany, to LandSat thermal mapper imagery and existing works on urban heat islands. Additionally we show how modifying the digital twin e.g. by adding trees or water areas allow the simulation of different scenarios to support decision-makers on their path towards resilient cities.

1. Introduction

The summer of 2025 brought extreme heat waves from June to July in whole Europe with temperatures from 46°C in Spain and Portugal up to 50.5°C in Turkey (Copernicus, 2025). Moreover increasing urbanization and densification reduce cooling green spaces in cities lead to so called urban heat islands (UHI) with increased surface- and air-temperatures in urban areas relatively to the surrounding rural areas. High temperatures are the reason for nearly 70 % of all summer deaths as shown in (Barnes et al., 2025) for the heatwave in mid 2025 with about 16000 excess deaths in 854 cities. Satellite earth observation allows to monitor the development of urban heat islands (Mekhloufi et al., 2025) to warn inhabitants early from dangerous heat. An other important way is increasing the resilience of cities to heat waves. For this we developed a simple but efficient method for the simulation of urban surface- and air-temperatures from only one single very high resolution stereo satellite scene from any location on the world (Krauß and Lindermeir, 2025).

For the simulation first a dense digital surface model (DSM) is calculated from the satellite stereo images to derive objects like buildings and trees. Using also the multi-spectral information from the satellite imagery gives a coarse classification of different surface materials and in turn allows the generation of an urban digital twin (DT) consisting of urban objects like buildings, trees, roads, water-bodies etc. which can be used for simulation purposes.

Deriving the sky-view for each point and shadows for each time of a specified day allows the simulation of temperatures in the air, on and below surfaces for the whole scene over this day. In this paper we compare the results of the simulation with ground truth information from the city of Memmingen (10.07° N, 47.98° E) to calibrate and validate the method. Furthermore we do second cross-checks with LandSat thermal imagery and an other operational method for mapping urban heat islands all over the world.

Afterwards we modify the digital twin derived from the satellite imagery to show how different scenarios can be simulated. Finally we discuss the results and give an outlook how the method can be improved and operationalized.

2. Existing simulation methods

Actually most methods for simulation of urban temperatures are based on computational fluid dynamics (CFD) or on the Weather Research and Forecasting model (WRF). The second method is designed for the use of large scale areas and not for fine urban structure analysis (Zhu et al., 2024). So we concentrate more on the existing Computational fluid dynamics models which are the base of most of all urban simulations involving thermal radiation, transfer, conduction and convection (Du et al., 2022). These methods deliver fine grained wind flow and thermal simulations for the modelled areas. But on the other hand these models need details like the numbers and locations of windows or the materials and colors of walls and much more which makes the set-up of them very tedious.

Actually PALM (Maronga et al., 2015) is one of the most commonly used tools for simulation of urban atmospheric boundary layers developed as a turbulence-resolving large-eddy simulation (LES) model based also on the Reynolds-averaged Navier-Stokes (RANS) equations. So it’s actually the state-of-the-art simulation but it needs also – as every CFD model – a very complex modeling and setup.

This contribution has been peer-reviewed. The double-blind peer-review was conducted on the basis of the full paper.
https://doi.org/10.5194/isprs-annals-XI-2-2026-907-2026

So we decided to start from scratch and implement a new, simplified model which is based only on one satellite image and a digital surface model (DSM) or a pair of satellite images. All needed parameters for an admittedly much simpler but never the less sufficient urban heat simulation are automatically derived in our proposed approach from the single satellite input data. Since we want to estimate a “worst case scenario” we ignore in our simulation the effects of detailed wind analysis and such the need for complex in-detail CFD simulations.

3. Data

Since we have access to in-situ-measurements of 72 temperature sensors scattered over the city area of Memmingen in Germany we decided to use this area as calibration and validation site. The sensors measure the air-temperature and relative humidity in a height of about 3 to 4 m above ground every 15 minutes. For this area also an Ikonos-stereo-pair acquired on 2008-08-30 at 10:26 UTC (© EUSI European Space Imaging, 2008) and two overlapping scenes from the french Pléiades satellite from 2023-06-25 at 10:13:48 and 10:13:58 where available (© Pléiades satellite imagery data 2023, property of Centre National d’Etudes Spatiales (CNES), provided by BKG and BMI through GAF, all rights reserved) as shown in fig. 1. While the Ikonos image pair has a fair stereo angle of about 30° with one scene looking nearly Nadir and a ground sampling distance of 90 cm the Pléiades “image pair” is in fact only the overlap area of two parallel acquired strips both looking to south-west and having only a stereo angle of 2° with a ground sampling distance of 60 cm. Both image pairs were processed and resampled to surface models and ortho images of a ground sampling distance of 50 cm.

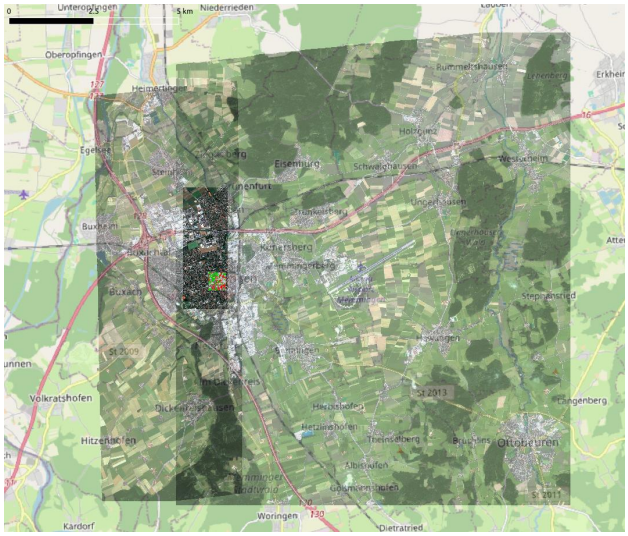

Figure 1. Test region Memmingen, Pléiades (left) and Ikonos (right) scene overlaid on OSM data, the test-area in the overlap-area (1.3×3.5 km^2) and the area of the details shown below overlaid as class-image (500×500 m^2).

In the following sections the Pléiades data and therefrom derived information is used for illustration if not mentioned otherwise. Fig. 2 shows the full DSMs derived from the Pléiades and Ikonos stereo-pairs.

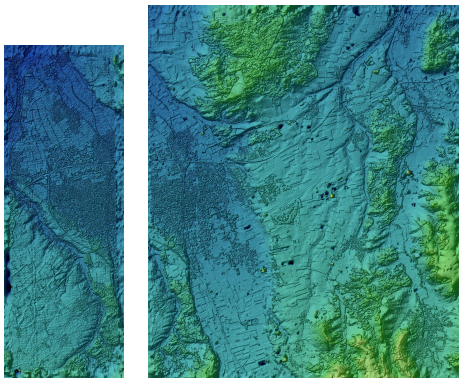

Figure 2. Digital surface models for the Pléiades (left, 4.4×12.4 km^2) and Ikonos (right, 11.6×13.9 km^2) stereo-pair.

4. Method

The presented method is based only on one single stereo scene of a very high resolution satellite like WorldView, Pleiades or Ikonos with a ground sampling distance of about 30 cm to below 1 m. From these images first a dense digital surface model (DSM) is derived. In turn a digital terrain model (DTM) containing only the ground without high objects like buildings or trees can be extracted. The difference of the DSM and DTM gives the normalized digital elevation model (nDEM) which contains the heights of objects above the ground as shown in fig. 3.

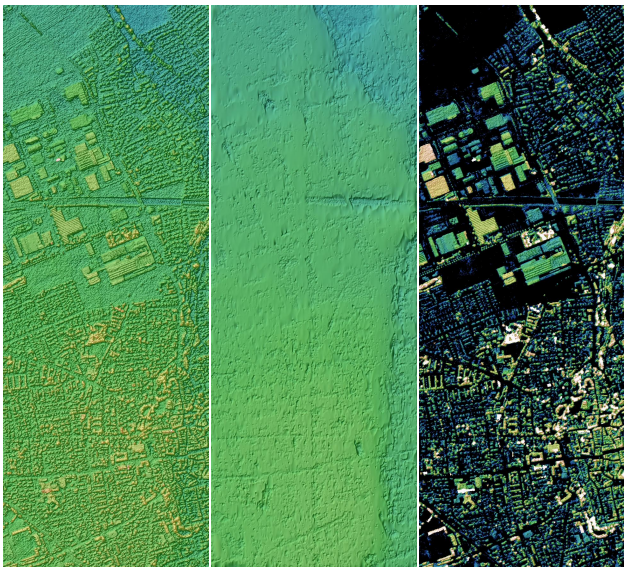

Figure 3. Test region Memmingen, 1.3×3.6 km^2, left: DSM, center: DTM, right: nDEM.

In parallel the panchromatic and multi-spectral satellite images are projected to the derived DSM to generate true-ortho-images. Fusing and merging these true-ortho-images give a pan-sharpened ortho image fitting exactly on ground.

This ortho image is subject to the spectral classification and allows together with the nDEM the derivation of the main classes water, tree, grass, soil, road, adobe-tiles and concrete. Based on the nDEM and the classification a so called digital twin (DT) of the area can be derived containing the ground and individual objects sitting on the ground.

For the simulation we apply to each of the – few but representa-

This contribution has been peer-reviewed. The double-blind peer-review was conducted on the basis of the full paper.
https://doi.org/10.5194/isprs-annals-XI-2-2026-907-2026 | © Author(s) 2026. CC BY 4.0 License.

tive – derived classes physical constants like the heat-capacity c in [kJ/kg/K], the heat-transport λ in [W/m/K], the density of the material ϱ in [kg/dm^3], the absorption α (in %) and the diffusion resistance r_l in [s/m].

In a next step based on the DSM the sky-view is calculated together with shadows every 300 seconds for a whole day. Using the derived shadows and the sky-view we can simulate the sun illumination – optionally moderated by weather conditions like clouds – for any given day.

Applying the sun illumination we calculate the incoming radiation (direct and indirect sunlight) and the outgoing (thermal) radiation. Using also the derived material-classes we are able to simulate heat-convection, heat-conduction and – if it’s not a dry surface – also the evaporation of the surface. Finally the thermal simulation runs several times for the day until stability is reached. The results are temperature maps for every 5 minutes for a whole day of 24 hours and temperature values for each minute at specified points for the whole day.

4.1 Preprocessing of the satellite data

After importing the satellite stereo pair the digital surface model (DSM) is derived using the semi-global-matching as shown in (dAngelo and Reinartz, 2011) (see fig. 3 above). Further on we use only a small overlapping section of 1.3×3.6 km^2 contained in all available satellite-images for a better detailed illustration (see the inserted small class-image in fig.1).

Based on the DSM a digital terrain model (DTM) representing only the ground without elevated objects like buildings or trees is calculated from the DSM using the watershed-method described in (Krauß, 2025). Subtracting the DTM from the DSM gives the so called normalized digital elevation model (nDEM) which contains the heights of the objects above ground (see also fig. 3 above, the DTM in the center and the nDEM on the right).

Using the ground (DTM) and the modelled objects from the nDEM allows the generation of a digital twin (DT) of the area. This digital twin contains the modeled objects like trees or buildings together with their heights and materials in a manner which can be used for different kinds of simulations – e.g. add, remove or change objects and simulate what impact such changes will have.

Figure 4. Detail section of test region Memmingen, 500×500 m^2, left: True ortho image from the Pléiades-scene, center: DSM, right: derived classification (blue: water, light-green: grass, dark-green: tree, red: adobe roof tiles, light-gray: concrete on flat roofs, dark-grey: asphalt/road, yellow: bare soil).

The panchromatic and multi-spectral satellite images are projected to the DSM, fused and merged to create pan-sharpened true-ortho-images. Using these true-ortho-images and the nDEM a coarse classification of the satellite data is performed. Fig. 4 shows the test area in Memmingen. On the left the true-ortho image derived from the original Pléiades satellite images is displayed. In the center the derived DSM and on the right the classification.

4.2 Classification and materials

For the classification a normalized difference vegetation index (NDVI) is calculated to derive water and vegetation areas. Together with the object height from the nDEM and other spectral properties like hue and saturation together with slopes from the DSM and the object heights gives the following classes (see also fig. 4):

- water: NDVI low
- grass: NDVI high, height low
- tree: NDVI high, height high
- adobe: red, height high, slope not flat
- concrete: gray, height high, slope flat
- road: gray, height low, slope flat
- soil: soil-spectrum, height low

For each of these classes typical material parameters are estimated and stored in the materials map $M_{x,y}$ consisting of the five bands c (heat-capacity in [kJ/kg/K]), λ (heat-transport in [W/m/K]), ϱ (density of the material [kg/dm^3]), α (absorption of the surface material, unit-less $[0 \ldots 1]$, derived from the albedo of the true-ortho image), r_l (diffusion resistance in [s/m]). A value of 0 s/m for r_l represents a dry material and no evaporation term is taken into account. A value of 1 is typical for an open water surface while values of 200 to 2000 can be used for leaves of trees or grass.

4.3 Sky-view, normals and shadows

Beneath this material map also a shadow mask $S_{x,y,t}$, the sky-view $V_{x,y}$ and the surface normal $\vec{N}_{x,y}$ for each pixel of the DSM are generated for the simulation. The shadow mask is calculated for t every 300 s from sun-rise to sun-set. The sky-view is a value from $0 \ldots 100$ % representing the portion of the sky which can be seen from this point in the DSM. It is used for calculation of the value of the indirect illumination and also for attenuation of small air-convection, which in turn is needed for cooling of dry surfaces and the evaporation of wet surfaces or plants.

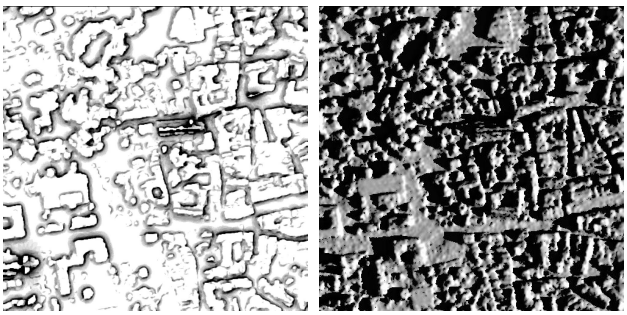

Figure 5. Detail 500×500 m^2, left: sky-view in percent (100 %: white, 0 %: black), right: sun-view at 7:00 UTC, same percentage range including shadows, indirect and direct lambertian irradiation.

The normals are needed for the calculation of lambertian direct illumination of a surface. From shadow and normals the sun-view as shown in fig. 5 (right) is calculated, which represents the percentage of the direct solar irradiance at each point. A face perpendicular to the sun-direction has a value of 100 %, a face in the shadow or parallel to the sun-direction receives 0 % of the sun illumination.

4.4 Simulation of temperatures

As described in (Krauß and Lindermeir, 2025) the simulation is based on a multi-layer temperature profile image of the same size as the inputs consisting of a surface layer and five substrate-layers of a depth of $d_s = 0.5$ m each below the surface and also five air-layers of $d_a = 2$ m each above the surface (see fig. 6). The surface and substrate layers have for each pixel (x, y) the unique material constants from the material map. All air-layers are modeled with the same physical constants for “air” independent of the position in the image.

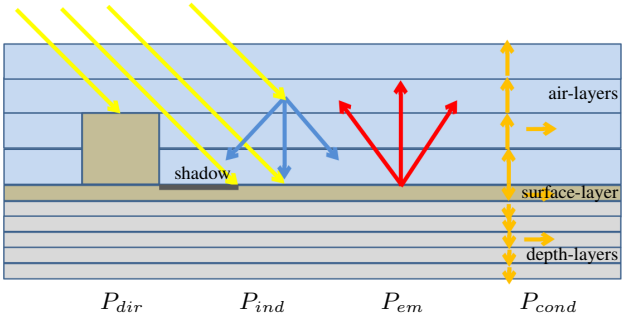

Figure 6. Illustration of the model used with one surface-layer and air- and depth-layers of different depths (in the simulation each 5 air- and depth-layers are used).

After initialization to a typical default temperature (e.g. 8 °C) the simulation calculates iteratively the heat (= energy) flow $\Delta Q = P \cdot \Delta t$ for each time-step Δt with P (in [W = J/s]) consisting of

P_{dir} the direct incoming radiation in non-shadow areas,
P_{ind} the indirect radiation also in shaded areas depending on the sky-view-factor,
P_{em} the thermal emission and also the loss of heat due to evaporation,
P_{cond} the heat-conduction in the material and heat-convection in the air-layers.

changing the temperature $T_{i,l,x,y}$ of every point (x, y) in each of the temperature-layers l using

$$T_{i+1} = T_i \cdot \frac{P \cdot \Delta t}{c \cdot m} \tag{1}$$

with the heat-capacity $c_{x,y}$ of surface pixel (x, y) in [kJ/kg/K] and the mass of this surface-pixel as $m = \varrho_{x,y} \cdot A \cdot d_s$.

Fig. 5 shows a detail of the simulation. On the left the sky-view can be seen. It’s the amount of sky which can be seen from one point on ground and ranges from 0 to 100 %. This sky-view is also a measure for the indirect radiation a point receives. On the right the final sun-view is shown which gives the incoming solar radiation consisting of (a) the local shadow at this time and point, (b) the direct solar radiation modified by the local slope and azimuth of the surface in this point and (c) of the indirect illumination depending on the solar elevation and the sky-view at this point.

5. Results

Fig. 7 shows the section of the classification image with the available temperature sensors for ground truth measurements. The five sensors used later in this section are annotated with their names. The color of the place-marks represent the temperatures at 2025-08-11, 10:04 UTC for comparison with the corresponding available LandSat thermal image. Each of the sensor measures the temperature in a height of about 3.6 m above the ground.

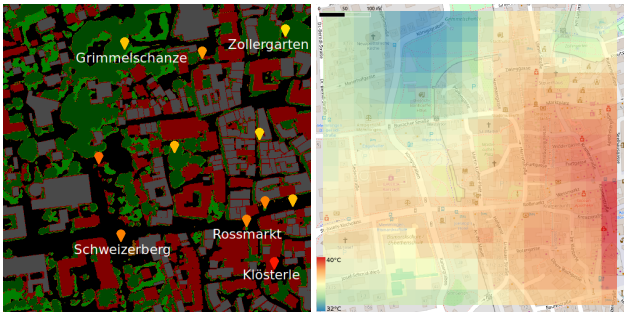

Figure 7. Left: Temperature sensors available in test area, the further used ones with names, right: surface temperatures of same area for 2025-08-11, 10:04 UTC.

The simulation runs typically one hour for the full test area of 1.3×3.5 km^2 with a resolution of 50 cm on a default laptop (Ubuntu 22.04, 2.8 GHz, 32 GB RAM) on a single core. The run-time is also depending on the time step (one shadow every 300 seconds), the days to iterate before the final result (3 days) and if evapotranspiration is included in the simulation (yes, otherwise the simulation time will drop to 20 minutes).

5.1 Evaluation using ground truth from temperature sensors

The results for sealed surfaces are shown in fig. 8. The simulation was running three days before the simulation day to gain stability.

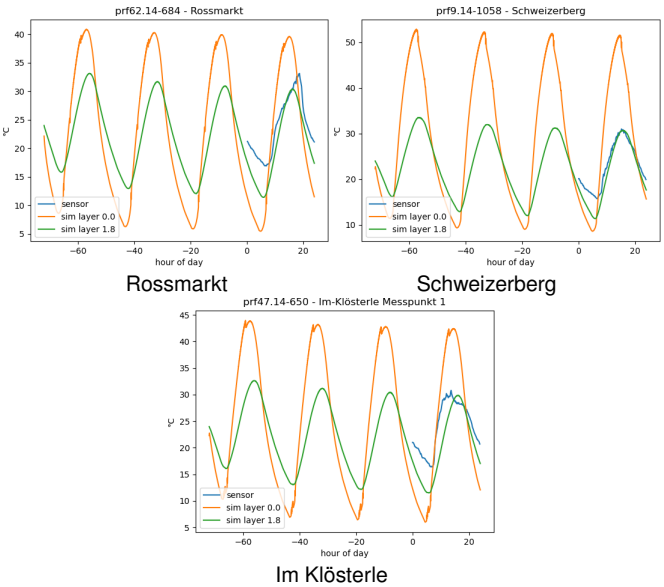

Figure 8. Results for stations “Rossmarkt”, “Schweizerberg” and “Im Klösterle”, blue: measurements of 2025-08-11, orange: simulation results of surface layer, green: simulation results at height of sensor above ground.

Three values are shown in all of these plots:

- blue: the measured temperature values of this sensor (ground truth)

This contribution has been peer-reviewed. The double-blind peer-review was conducted on the basis of the full paper.
https://doi.org/10.5194/isprs-annals-XI-2-2026-907-2026 | © Author(s) 2026. CC BY 4.0 License.

- orange: the simulated surface temperature at this point
- green: the simulated air temperature at this point measured in the height of the sensor

As can be seen in fig. 8 stability of the simulation was reached early and stays relatively constant for the four days. The final simulation run for the last day shows a very good correlation with the measured temperatures of the sealed areas.

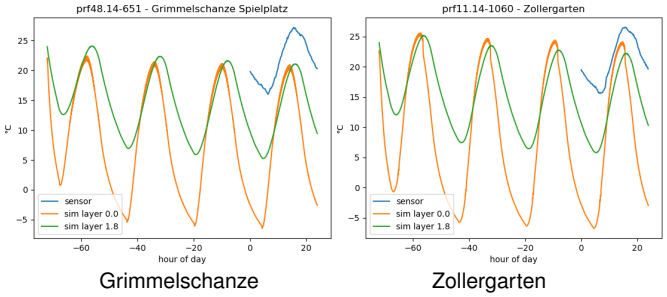

Figure 9. Results for stations “Grimmelschanze” and “Zollergarten”, blue: measurements of 2025-08-11, orange: simulation results of surface layer, green: simulation results at height of sensor above ground.

Fig. 9 shows the simulation results for two measurement points in park areas. As can be seen the differences between the surface temperatures (orange) and the air-temperatures (green) vanish almost in tree covered areas. The exact position and surface of the sensor “Grimmelschanze” (which in fact is named “Grimmelschanze Spielplatz” – playground area) could not be validated in the satellite data. The associated position of this sensor is located on a tree in the satellite image. But due to the appendix “playground area” we assume it’s not in the tree but rather on a open space near ground which may explain the higher sensor measurements.

Looking at the other park area sensor “Zollergarten” the reference point is located beneath trees but on a vegetation covered ground. So this may explain the better correlation for this sensor.

Considering the coarse estimation of the diffusion resistance of the trees in gathering the material constants and also the unavailable wind speed and humidity during the simulation time which are all involved in calculating the evaporation of vegetated areas the results can be assumed as acceptable. This even more if the behaviour of the simulation in vegetated areas like “Zollergarten” (fig. 9, right) and sealed areas like in e.g. “Schweizerberg” (fig. 8, top right) show the typical differences between the surface temperatures and the air temperatures of such areas. On sealed surfaces the surface temperature (orange plot) is typically much higher than the air temperature (green plot) while both temperatures beneath trees are typically nearly the same.

The next simulation was done for 2025-01-14. As shown in fig. 10 there were about 50 % clouds in the night so the simulation was conducted with the extra parameters “cloudcover=50,0,50” and “no evaporation” (due to winter-time).

The results for the only available three measuring points at this date from our test-area are shown in fig. 11. Interestingly the results for the sealed areas match perfectly also reveiling no large differences between the surface temperature and the air temperature in the sensor height of about 3.6 m. Additionally it’s worth

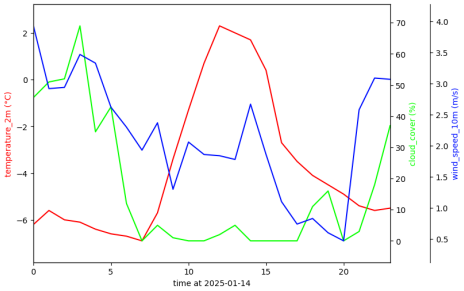

Figure 10. Weather data for 2025-01-14 from open-meteo.com.

mentioning that the resulting air temperatures match perfectly the measured lowest night as also the highest day temperatures. The result for the park area “Grimmelschanze” shows in contrast a much higher surface temperature and still a little to high air temperature of the simulation at the measuring station but a perfect match for the lowest night temperature just before sunrise.

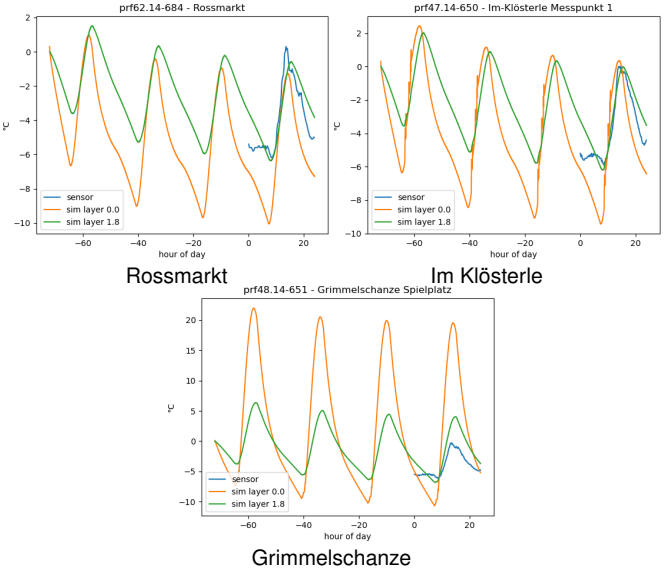

Figure 11. Results for 2025-01-14 at stations “Rossmarkt”, “Im Klösterle” and “Grimmelschanze”, blue: measurements of 2025-01-14, orange: simulation results of surface layer, green: simulation results at height of sensor above ground.

As a conclustion of the comparison of the simulation results to the actual measured temperatures of the in-situ temperature sensors a very good correlation can be found. So the “calibration” step mentioned above can just be skipped, since the simulation results fit alread to the really measured temperatures. The only point to take into account is to not use the surface temperature of the simulation (layer 0) but the air-layer in a height corresponding to the height of the sensor above ground: air-layer 1.8 for the sensor height at 3.6 m.

5.2 Evaluation using LandSat thermal imagery

In fig. 12 the LandSat thermal image for 2025-01-14, 10:10 UTC is shown on the left side while the corresponding simulation for the whole area is shown at the center and the downsampled simulation result on the right side. As can be seen the surface temperatures match very well (figs. 12 and 13 share the same temperature-scale for comparison).

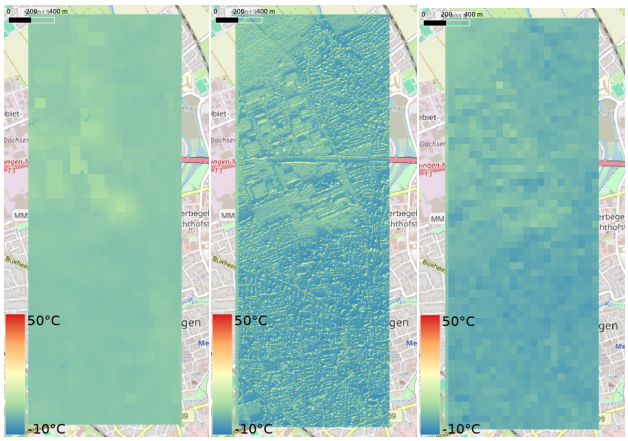

Figure 12. LandSat thermal image (left), simulation result (center) and down-sampled simulation result (right) for 2025-01-14, 10:10 UTC.

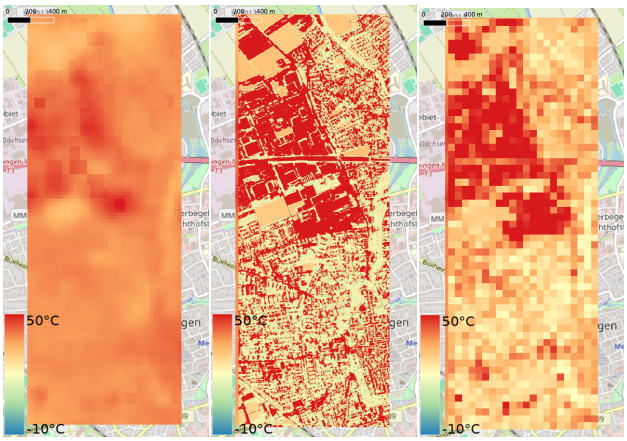

Figure 13. LandSat thermal image (left), simulation result (center) and down-sampled simulation result (right) for 2025-08-11, 10:04 UTC.

Table 1 shows the temperature statistics of the LandSat image, the corresponding simulation and also the simulation result down-sampled to the native resolution of the LandSat thermal band (60 m). The statistics show a nearly perfect match of the average surface temperature for the whole test area in January. The minimum and maximum temperatures for the high resolution simulation are more extreme than the satellite data values which is justified by the different pixel area sizes over which the information is integrated. Comparing the LandSat statistics to the down-sampled simulation shows how the minimum and maximum values come closer to the LandSat data.

Image	Month	Minimum	Maximum	Average
LandSat	1	-3.6°C	3.2°C	-1.5°C
Simulation	1	-8.5°C	19.5°C	-2.0°C
Sim 60 m	1	-6.4°C	4.0°C	-2.0°C
LandSat	8	27.7°C	47.0°C	35.4°C
Simulation	8	-1.7°C	65.0°C	31.8°C
Sim 60 m	8	15.0°C	59.5°C	31.8°C

Table 1. Surface temperature statistics for the LandSat thermal image and the simulation of 2025-01-14, 10:10 UTC and 2025-08-11, 10:04 UTC respectively.

Comparing the results of the simulation with the LandSat thermal image from 2025-08-11, 10:04 UTC in table 1 reveals a slightly inferior statistical result originating from too low night temperatures as discussed later. Fig.13 shows the LandSat thermal image and the simulation for 2025-08-11, 10:04 UTC.

In table 2 temperatures T_{LS} for the five measurements points are extracted from the LandSat image of 2025-08-11 (c.f. fig. 7, right) and also the simulated surface temperatures T_{sim} for the surface at 10:04 UTC extracted from the simulation.

Measuring point	T_{LS}	T_{sim}
Rossmarkt	38.0°C	35.2°C
Schweizerberg	36.9°C	37.9°C
Klösterle	38.2°C	29.6°C
Grimmelschanze	31.8°C	18.6°C
Zollergarten	35.1°C	19.1°C

Table 2. Surface temperatures measured from the LandSat thermal image of 2025-08-11, 10:04 UTC, converted to degree Celsius and comparison with resulting surface temperatures from the simulation at this time.

As can be seen the simulated surface temperatures of sealed areas are in the range of 30 to 38°C while for park areas they are around 19°C. The surface temperatures extracted from the LandSat thermal image range from 37 to 38°C for sealed areas and from 32 to 35°C in park areas. Especially the last – Zollergarten – shows a much higher temperature as expected. But these effects can be explained by comparing pixel resolutions of the simulation and the LandSat imagery. While the simulation works on a pixel size of 1 m the native resolution of the thermal band of the LandSat satellite is 60 m down-sampled to 30 m in the image used. So the enclosed small park Zollergarten gets dominated by the temperatures of the buildings around.

Comparing the simulation and the measurements show also temperatures typically about 5 K too low in the summer simulation for the early morning hours before sun rise. There are two explanations which has to be checked further:

- Back-scatter-ratio: the back-scatter ratio T_{back} of the atmosphere is typically about 0.65-0.75 – in the simulation a mean value of 0.7 was used (this back-scatter ratio increased during the last sixty years due to more CO_2 in the atmosphere, which effect was already described in (Arrhenius, 1896)).
- Clouds: there may be clouds over the night, so the temperature loss by black-body-radiation during the night is overestimated (the back-scatter ratio T_{back} of the atmosphere increases up to 0.95 if there are clouds)

5.3 Evaluation using SUHI

In (Richiardi et al., 2025) a method is presented for calculation of surface urban heat island (SUHI) from LandSat satellite data for each city around the world. The detailed workflow is shown in fig. 14.

Fig. 15 shows the results of the calculated thermal anomaly for the surface urban heat island in the area of Memmingen.

Using the down-sampled simulation results for 2025-01-14 and 2025-08-11 we can also calculate heat-anomaly for these images and compare them to the thermal anomaly as shown in fig. 16.

As can be seen in fig. 16 the urban heat island thermal anomaly for the simulated dates in January and August show higher

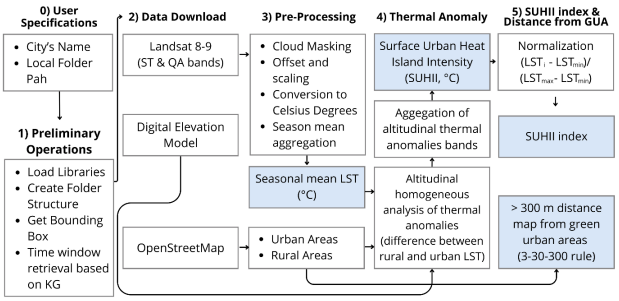

Figure 14. Workflow of the calculation of the surface urban heat island index showing the thermal anomaly between urban areas and their surroundings.

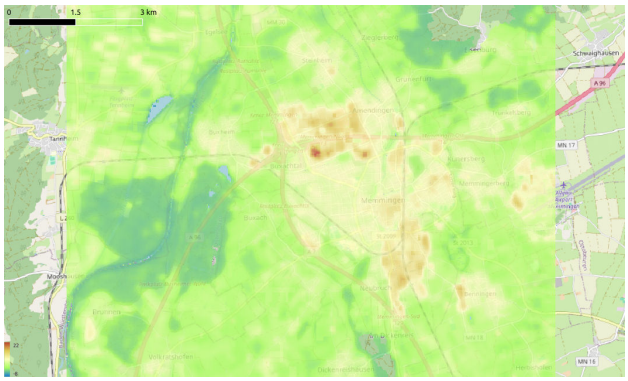

Figure 15. The surface urban heat island thermal anomaly around Memmingen (section 14×8 km^2) ranging from -8 K (dark blue) to 22 K (red).

anomalies than the surface urban heat island thermal anomaly map from (Richiardi et al., 2025). But the January and August simulations are extreme winter and summer examples. To get a more valid anomaly map the simulation should be run for more days around a whole year including also different typical cloud coverage scenarios at day and night (regression to the mean).

6. Changing the Scenario

The simulation based on the digital twin (DT) allows also to analyse new scenarios – e.g. what happens if there are trees planted on an actually sealed square or if water areas are created in the urban area. For this the workflow described in 4.1 allows overwriting the DSM and classification by adding a vector layer containing new objects and scenario information like a class and height for each object. This in turn changes the generated digital twin, the material map and finally also the DSM from which the sky-view and shadow is derived.

In this section we insert some trees and also a water area in the existing model as shown in fig. 17, run the simulation and analyze the changes.

Fig. 18 shows the simulated surface temperatures for 2025-08-11 at times 5:00, 9:00, 13:00 and 17:00 UTC. The top row contains the original simulation results and the bottom row the simulation of the changed scenario. Especially the noon and afternoon images show the important temperature reduction due to the inserted trees at Schweizerberg (left) and the massive change around the newly inserted lake at Rossmarkt (right).

For a more detailed analysis fig. 19 shows the temperature graphs over time at the measuring stations “Schweizerberg”

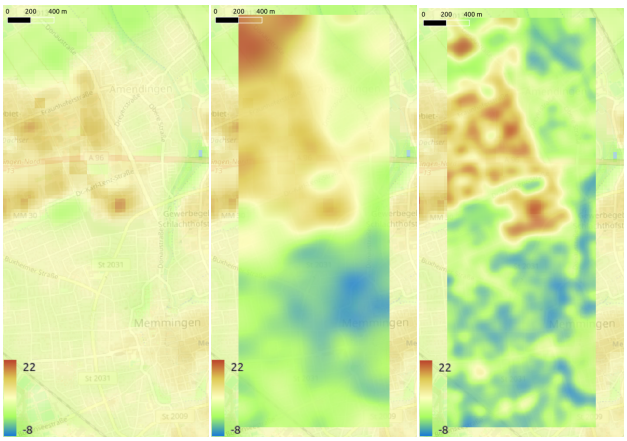

Figure 16. Comparison of the surface urban heat island thermal anomaly (left) and the thermal anomalies calculated from the simulations for 2025-01-14 (center) and 2025-08-11 (right).

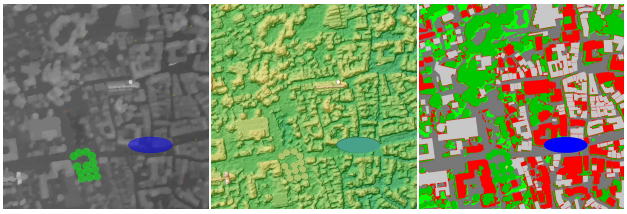

Figure 17. Changed scenario: trees planted near “Schweizerberg” and a new lake near “Rossmarkt” (left), DSM (center) and new digital twin classes (right).

(left) and “Rossmarkt” (right). The top row contains again the original scenario and the bottom row the modified scenario. Looking at the surface and air temperatures at “Schweizerberg” it can be seen, that the simulated surface temperature drops from 55°C to 31°C and the simulated air temperature from 32°C to 26°C due to the inserted trees. At the station “Rossmarkt” the simulated surface temperature drops from 42°C to 20°C and the simulated air temperature from 32°C to 23°C near the added lake. The surface temperature is interestingly near the lake lower than the air temperature which can be explained with the convection of warmer air over the lake to the lake borders.

7. Conclusion and outlook

In the presented work we described a simplified approach for simulating temperatures over an urban area solely using a very high resolution satellite image stereo-pair as inputs. From the

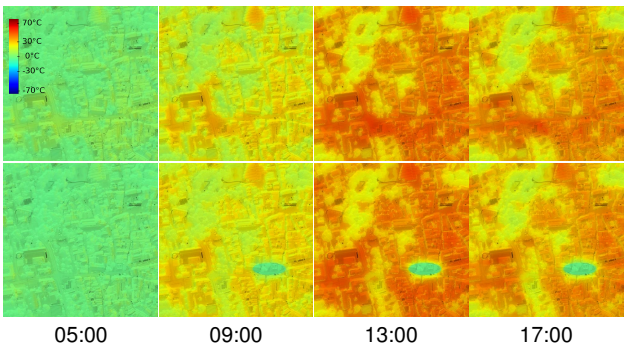

Figure 18. Simulated temperatures for original scenario (top) and modified scenario (bottom)

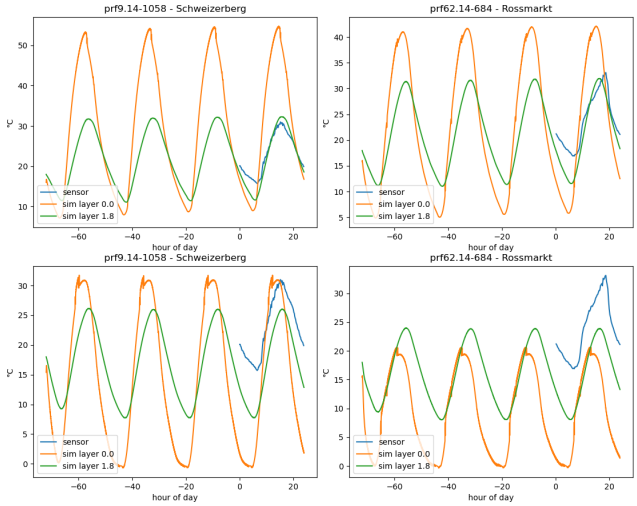

Figure 19. Simulated temperatures for “Schweizerberg” (left) and “Rossmarkt” (right), top: original scenario, bottom: modified scenario

satellite data a digital surface model (DSM) and also a simplified material classification is derived. Using the DSM the shadows for every five minutes of a day can be calculated. Also slopes and the sky-view are derived. The material classification is based on the multi-spectral pan-sharpened true-ortho satellite image together with the slopes and the heights above ground. For each classified material typical physical values like density, absorption, heat conduction, heat capacity and diffusion resistance are stored in the materials-map.

In a second step the simulation runs on these derived physical material data building up a surface layer and a number of substrate- and air-layers. For each of the layers the temperature is iterated calculating incoming and outgoing radiation, heat flows, heat conduction, convection and the transpiration of wet surfaces – especially the leaves of trees.

Comparing the results to in-situ measurements and also to surface temperature maps from LandSat thermal mapper imagery and thermal surface urban heat island anomalies show a good correlation over the test area.

The simulation makes it also possible to test different scenarios like adding trees or replacing buildings with water areas. The presented simulation results of the original digital twin and the modified scenario make the simulation valuable for urban planning tasks.

For a better refinement and calibration of the model it should be evaluated with more in-situ temperature measurements of different cities in different climate zones around the world.

Acknowledgments

We thank the city of Memmingen for providing measurements of temperature sensors in Memmingen as ground truth data. Also we thank the German federal cartographic institute (BKG) and GAF for providing the Pléiades data and the DLR archive and European Space Imaging for access to the Ikonos data.

References

Arrhenius, S., 1896. On the influence of carbonic acid in the air upon the temperature of the ground. *Philosophical Magazine and Journal of Science*, 5th series(41), 237-76.

Barnes, C., Konstantinoudis, G., Masselot, P., Mistry, M., Gasparrini, A., Vicedo-Cabrera, A. M., Theokritoff, E., Clarke, B., and, F. O., 2025. Summer heat deaths in 854 European cities more than tripled due to climate change. Technical report, Imperial Grantham Institute.

Copernicus, 2025. Surface air temperature for July 2025. `https://climate.copernicus.eu/surface-air-temperature-july-2025`. (accessed 10/2025).

dAngelo, P., Reinartz, P., 2011. Semiglobal Matching Results on the ISPRS Stereo Matching Benchmark. *International Archives of Photogrammetry and Remote Sensing*, XXXVIII-4/W19, 79–84.

Du, S., Zhang, X., Jin, X., Zhou, X., Shi, X., 2022. A review of multi-scale modelling, assessment, and improvement methods of the urban thermal and wind environment. *Building and Environment*, 2013, 108860. `https://www.sciencedirect.com/science/article/pii/S0360132322001068`.

Krauß, T., 2025. Generation of Digital Terrain Models from Digital Surface Models using a Watershed Transformation Approach. A. Christofi, D. G. Hadjimitsis, S. C. Michaelides, K. Themistocleous, C. Danezis, N. Kyriakides, G. Papadavid, V. Ambrosia, F. Schwandner, A. Anayiotos, I. Gitas (eds), *Eleventh International Conference on Remote Sensing and Geoinformation of the Environment (RSCy2025)*, 13816, International Society for Optics and Photonics, SPIE, 138160B.

Krauß, T., Lindermeir, E., 2025. Simulation of urban temperatures from very high resolution satellite imagery. *2025 Joint Urban Remote Sensing Event (JURSE)*, CFP25RSD-ART, 1–4.

Maronga, B., Gryschka, M., Heinze, R., Hoffmann, F., Kanani-Sühring, F., Keck, M., Ketelsen, K., Letzel, M. O., Sühring, M., Raasch, S., 2015. The Parallelized Large-Eddy Simulation Model (PALM) version 4.0 for atmospheric and oceanic flows: model formulation, recent developments, and future perspectives. *Geosci. Model Dev.*, 8, 1539-1637. `https://palm.muk.uni-hannover.de/`.

Mekhloufi, N., Aquilino, M., Baziz, A., Richiardi, C., Adamo, M., 2025. Free satellite data and open-source tools for urban green spaces and temperature pattern analysis in Algiers. *International Journal of Applied Earth Observation and Geoinformation*, 139, 104482. `https://www.sciencedirect.com/science/article/pii/S1569843225001293`.

Richiardi, C., Caroscio, L., Crescini, E., De Marchi, M., De Pieri, G. M., Ceresi, C., Baldo, F., Francobaldi, M., Pappalardo, S. E., 2025. A global downstream approach to mapping surface urban heat islands using open data and collaborative technology. *Sustainable Geosciences: People, Planet and Prosperity*, 2025(100006). `https://www.sciencedirect.com/science/article/pii/S2950492925000057`.

Zhu, H.-C., Ren, C., Wang, J., Feng, Z., Haghighat, F., Cao, S.-J., 2024. Fast prediction of spatial temperature distributions in urban areas with WRF and temporal fusion transformers. *Sustainable Cities and Society*, 103, 105249.